AD_____

Award Number: W81XWH-09-1-0410

TITLE: Harnessing the Power of Light to See and Treat Breast Cancer

PRINCIPAL INVESTIGATOR: Nimmi Ramanujam, Ph.D.

CONTRACTING ORGANIZATION: Duke University
                                                Durham, NC 27708

REPORT DATE: October 2011

TYPE OF REPORT: Annual

PREPARED FOR: U.S. Army Medical Research and Materiel Command
                        Fort Detrick, Maryland 21702-5012

DISTRIBUTION STATEMENT: Approved for Public Release;
                                          Distribution Unlimited

REPORT DOCUMENTATION PAGE

Form Approved
OMB No. 0704-0188

Public reporting burden for this collection of information is estimated to average 1 hour per response, including the time for reviewing instructions, searching existing data sources, gathering and maintaining the data needed, and completing and reviewing this collection of information. Send comments regarding this burden estimate or any other aspect of this collection of information, including suggestions for reducing this burden to Department of Defense, Washington Headquarters Services, Directorate for Information Operations and Reports (0704-0188), 1215 Jefferson Davis Highway, Suite 1204, Arlington, VA 22202-4302. Respondents should be aware that notwithstanding any other provision of law, no person shall be subject to any penalty for failing to comply with a collection of information if it does not display a currently valid OMB control number. **PLEASE DO NOT RETURN YOUR FORM TO THE ABOVE ADDRESS.**

1. REPORT DATE	2. REPORT TYPE	3. DATES COVERED
October 2011	Annual	18 September 2010 – 17 September 2011

4. TITLE AND SUBTITLE

Harnessing the Power of Light to See and Treat Breast Cancer

5a. CONTRACT NUMBER

5b. GRANT NUMBER
W81XWH-09-1-0410

5c. PROGRAM ELEMENT NUMBER

6. AUTHOR(S)

Nimmi Ramanujam, Ph.D.

E-Mail: nimmi@duke.edu

5d. PROJECT NUMBER

5e. TASK NUMBER

5f. WORK UNIT NUMBER

7. PERFORMING ORGANIZATION NAME(S) AND ADDRESS(ES)

Duke University
Durham, NC 27708

8. PERFORMING ORGANIZATION REPORT NUMBER

9. SPONSORING / MONITORING AGENCY NAME(S) AND ADDRESS(ES)
U.S. Army Medical Research and Materiel Command
Fort Detrick, Maryland 21702-5012

10. SPONSOR/MONITOR'S ACRONYM(S)

11. SPONSOR/MONITOR'S REPORT NUMBER(S)

12. DISTRIBUTION / AVAILABILITY STATEMENT
Approved for Public Release; Distribution Unlimited

13. SUPPLEMENTARY NOTES

14. ABSTRACT

Our objective is to exploit the wealth of physiological, metabolic, morphological and molecular sources of optical contrast to develop novel strategies that focus on two breast cancer applications: tumor margin assessment and prediction of response to neo-adjuvant therapy. The proposed aims of this grant are expected to result in three major contributions. The first has the most immediate impact. An optically based strategy that can quickly and non-destructively detect positive tumor margins will decrease the need for re-excision surgery and thereby decrease the local recurrence rate and rate of distant metastases in women electing BCS. Gaining insight into the physiological, metabolic, morphological and molecular sources of heterogeneity within and among tumors and how they are modulated by therapy, drug resistance and metastatic potential will directly benefit prognostication, prediction of outcome and planning of cancer therapies. With these tools, clinicians and clinical researchers can get a better understanding of this disease and how it might react to a drug. Basic science researchers could use it as an informed approach to study tumor biology and assay the effect of novel therapeutic agents in vivo.

15. SUBJECT TERMS
optical spectroscopy, imaging, fiber-optic, molecular, screening, breast cancer

16. SECURITY CLASSIFICATION OF:			17. LIMITATION OF ABSTRACT	18. NUMBER OF PAGES	19a. NAME OF RESPONSIBLE PERSON USAMRMC
a. REPORT	b. ABSTRACT	c. THIS PAGE	UU	34	19b. TELEPHONE NUMBER (include area code)
U	U	U			

Table of Contents

1. INTRODUCTION:

Our objective is to exploit the wealth of physiological, metabolic, morphological and molecular sources of optical contrast to develop novel strategies that focus on two breast cancer applications: tumor margin assessment and prediction of response to neo-adjuvant therapy. The proposed aims of this grant are expected to result in three major contributions. The first has the most immediate impact. An optically based strategy that can quickly and non-destructively detect positive tumor margins will decrease the need for re-excision surgery and thereby decrease the local recurrence rate and rate of distant metastases in women electing BCS. Gaining insight into the physiological, metabolic, morphological and molecular sources of heterogeneity within and among tumors and how they are modulated by therapy, drug resistance and metastatic potential will directly benefit prognostication, prediction of outcome and planning of cancer therapies. With these tools, clinicians and clinical researchers can get a better understanding of this disease and how it might react to a drug. Basic science researchers could use it as an informed approach to study tumor biology and assay the effect of novel therapeutic agents *in vivo*.

a. Original Statement of Work for 5 Years

Aim 1: Optical imaging of margin morphology on breast lumpectomy specimens: To evaluate the role of wide-field imaging (coverage) and high-resolution interrogation (localization) of breast margin morphology to guide surgical resection intra-operatively and pathologic assessment of the tumor margin post-operatively (Timeframe: year 1-5).
  1a. Development of one optical spectral imaging system that integrates sensing capabilities for aims 1 and 2 and a high-resolution probe that can image absorption, scattering and fluorescence contrast (timeframe, year 1).
  1b. Conduct clinical studies on lumpectomy margins on 200 patients (time frame, years 2-4)
  1c. Data analysis and interpretation (timeframe, years 3-5)
> Test the sensitivity and specificity of wide-field imaging to detect positive tumor margins
> Test sensitivity and specificity of high-resolution probe to detect IDC and DCIS.

Aim 2: Optical quantitative biology of different sub-types of breast cancer: To investigate biomarkers of oxygenation, carotenoids (β-carotene) and ECM proteins (collagen) in human breast cancer stratified by tumor sub-type and receptor status and their association with neo-adjuvant chemotherapy response.
  2a. Development of rotating needle compatible spectroscopy probe (timeframe, year 1).
  2b. Conduct clinical studies to measure optical biomarkers *in vivo* in 150 patients undergoing surgery (timeframe, years 2-4).
  2c. Conduct clinical studies to measure optical biomarkers from 75 patients before neo-adjuvant therapy
  2d. Data analysis and interpretation (years 3-5):
> Determine association of biomarkers with tumor subtype
> Determine association of biomarkers with receptor status
> Determine association of biomarkers with genomic signatures
> Determine association of biomarkers with pathologic sub-total and complete response

Aim 3: Optical quantitative biology to assess therapy response in different sub-types of breast cancer: To investigate biomarkers of oxygenation and ECM proteins (collagen and $\alpha_v\beta_3$ expression) in rodent breast cancer stratified by tumor sub-type, receptor status and metastatic potential in response to targeted and chemotherapies.

    3a. To determine if multi-parametric intra-vital optical microscopy, measuring hemoglobin saturation, total hemoglobin, redox ratio, collagen, and integrin expression can monitor tumor response to tamoxifen in parental and tamoxifen-resistant MCF-7 tumors in the mouse dorsal skin fold window chamber (timeframe, years 1-2).

        ▪ A total of 40 athymic nude mice will be required for this study (10 mice/group).

    3b. Monitor optical parameters in the dorsal skin fold window chamber in response to doxorubicin chemotherapy in MCF-7 parental and doxorubicin-resistant tumors (timeframe, years 2-3).

        ▪ A total of 40 athymic nude mice will be required for this study.

    3c. Monitor optical parameters in the dorsal skin fold window chamber in response to doxorubicin chemotherapy in tumors that express high (MDA-435) and low (MCF-7) levels of $\alpha_v\beta_3$ integrin (timeframe, years 3-4).

        ▪ A total of 40 athymic nude mice will be required for this study.

    3d. Data and statistical analysis (timeframe, year 5).

2. BODY

Aim 1: Optical imaging of margin morphology on breast lumpectomy specimens

In Aim 1, our objective is to develop a strategy for high resolution fluorescence imaging of tumor margins, and to combine that with wide-field diffuse spectral imaging in a complementary fashion. For the high resolution fluorescence imaging component of the project, last year we demonstrated the feasibility of high resolution fluorescence imaging for detection of residual carcinoma in the normal tissue milieu. Here we focus primarily on image analysis techniques and our quantitative approach for diagnosing high resolution anatomical images of heterogeneous tissue. To do so we are employing the use of two ex vivo test beds: 1) murine sarcoma margins and 2) human mastectomy specimens. Each of these approaches is subsequently discussed in more detail.

High Resolution Imaging

Introduction:
One strategy for accurate assessment of tumor margins is to adopt approaches that exploit features that are already leveraged in traditional pathology, such as nuclear size and density, and relationships between tumor cells and surrounding support structures (collagen, fat). There is evidence in the literature of the success of such approaches.[1-4] This compelling evidence, which is detailed in Table 1, suggests that high resolution imaging of the tumor microanatomy, in particular nuclei, can provide exquisite contrast for the detection of microscopic residual disease that could be effective across different cancers and patient demographics.

Table 1: High resolution technologies for in situ pathology

Group	Contrast	Technology	Context	Analysis
Farkas et al[1]	DAPI	Fluorescence microscopy	Ex vivo rat mammary tumor xenografts	Watershed algorithm (nuclear size, count)
Gareau et al[2]	Acridine orange	Confocal fluorescence microscopy	Skin excisions from Mohs	Human-observer
Gmitro et al[3]	Acridine orange	Confocal fluorescence microscopy	Ex vivo ovarian tissue	First order statistics, spatial frequency content
Kortum et al[4]	Acriflavine	Fluorescence microendoscopy	Esophageal biopsies	First order statistics, spatial frequency content

Most of these approaches focus on (1) epithelial sites in which the primary diagnostic feature is the size, spacing, and density of nuclei and (2) calculate statistical features related to the intensity information captured from raw images (entropy, variance, etc.). While these approaches work well for the detection of epithelial cancers, the translation of such approaches to heterogeneous tissue sites is limited. Additionally, it is difficult to interpret quantitative parameters such as variance and relate them directly to tissue morphology. Therefore, to address this limitation, we focus *on quantifying features that directly reflect tissue morphology in __highly heterogeneous tissues__ with the ultimate goal of developing a tool for __quantitative in situ pathology__ that can be used in combination with our wide field spectral platform to diagnose breast margins intra-operatively.*

Towards this end, we employ the use of a high resolution fluorescence microendoscope (HRME) combined with a fluorescent contrast agent called acriflavine developed by Rebecca Richards-Kortum at Rice Univeristy.[5] Unlike DAPI, acriflavine binds to cell nuclei as well as other support tissues such as collagen, elastin, and adipose tissues allowing for full visualization of the tissue microanatomy. Also, acriflavine is safe and is currently being used in humans under IND approval in the oral cavity and ovary.[6] The HRME, which consists of a LED, dichroic, emission filter, CCD, and coherent fiber bundle, was chosen because of it can resolve subcellular structures (such as nuclei), which is needed to recapitulate pathology, and because of its portability, low cost, and high SNR.[5]

Our ultimate goal is to use the wide field spectral platform to identify suspicious areas on a margin and then use the HRME imaging and subsequent quantitative analysis to assess margins intraoperatively. However, we acknowledge that detecting the small focal areas of residual cancer that characterize lumpectomy margins poses challenges and is therefore not the optimal setting in which to complete preliminary studies of high resolution imaging and quantitative analysis for surgical margins. Therefore, we first completed a preliminary study of HRME imaging and analysis in a transgenic murine sarcoma margin model, which was developed by our collaborator, David Kirsch.[7] This model was chosen because transgenic tumors are better suited for margin imaging than implanted or chemically induced tumors. Implanted tumors tend to grow within a fibrous capsule, and don't exhibit the problematic in-growths of tumor tissue into surrounding tissue that is characteristic of spontaneous tumors. Also, these models (including chemically-induced tumors) grow in immuno-deficient animals, which do not provide a normal tumor microenvironment.

Next we have applied our image analysis techniques to a cohort of HRME images captured from clinical mastectomy specimens. We chose to start with mastectomy specimens as

opposed to lumpectomy margins due to the increased yield of malignant samples that can be acquired from bisected mastectomies. Having a cohort of images that contains the breadth of normal tissue variants as well as malignant variants enables us to more appropriately evaluate the potential of our analytical imaging approach.

1) *Ex vivo* murine sarcoma margins study

Methods:
Imaging system. For this work, we used a high resolution fluorescence microendoscope (HRME) to collect high resolution microscopic images of stained tissues. The HRME device has previously been described in detail.[5] Briefly, the system contains a 455 nm light emitting diode (LED) to excite acriflavine, a dichroic mirror, emission filter, CCD camera, and coherent fiber bundle.

Mice and sarcoma generation. All animal work was performed in accordance with Duke University Institutional Animal Care and Use Committee approved protocols. The generation of the temporally- and spatially-constrained transgenic model of murine sarcoma is described in detail in Kirsch et al. Briefly, mouse genotypes used to generate sarcomas include LSL-KrasG12D/+;Trp53Flox/Flox, BrafCa/+;Trp53 Flox/Flox and BrafCa/Ca;Trp53Flox/Flox.[7,8] Soft tissue sarcomas were generated by intramuscular injection of a calcium phosphate precipitate of an adenovirus expressing the Crerecombinase (Gene Transfer Vector Core, University of Iowa).[7] For the ex vivo study, mice were euthanized immediately prior to surgical tumor resection and imaging. Seven animals were used in this study.

Ex vivo imaging protocol. Within ten minutes of euthanasia, tumor and normal tissue sections were removed. Sections were laid flat followed by topical application of 0.01% (w/v) acriflavine (Sigma-Aldrich) dissolved in phosphate buffered saline (PBS). After 30 seconds, the distal end of the HRME fiber bundle was placed in contact with the tissue and images were acquired. In a few cases frozen tissue slices mounted on glass slides were raster-scanned to create mosaics of the tissue face by systematically moving the probe in 1 mm increments in rows over the tissue surface. In order to improve the accuracy and reproducibility of these movements the fiber bundle was secured in a custom probe holder fiber chuck which was mounted on an x-y translation stage. The distal end of the probe was cleaned with 55% ethanol between each probe placement.

During the imaging session specific sites of interest were inked with 1 mm dots using histological inks to facilitate pathologic coregistration. The mosaic image acquisition was performed on frozen tissue sections in order to facilitate direct spatial coregistration with histopathology regions. After imaging and inking was complete, the tissue was submitted for fixing, paraffin-embedding and sectioning. The resulting hematoxylin and eosin (H&E) stained slides were reviewed by an expert oncology pathologist and an expert veterinary pathologist, both of whom were blinded to the results of HRME imaging. For each inked area, the tissue was diagnosed as tumor, muscle, adipose, or any combination thereof. For mosaics a diagnosis was given for the entire section.

Image analysis. Since the most clinically relevant goal is to detect the presence of microscopic disease, we focused our quantitative approach on first isolating features of interest, such as nuclei, and then calculating features that may be used to determine the presence of tumor cells in an image, such as the size and density of those nuclei. Our first step was to remove the fiber core pattern that is superimposed onto each image (since the images are discretely sampled through a fiber bundle) by applying a Gaussian filter to remove the high frequency content. This

step smoothed the image without removing spatial frequency information inherent to the tissue structure, and was done in order to remove the bias or artifact that the fiber pattern could introduce during subsequent image processing.

Next, in order to isolate the cell nuclei from other structures, such as muscle fibers or adipocytes, we utilized a sparse decomposition algorithm. This approach is based on sparse component analysis, which to our knowledge has never been applied to high-resolution anatomical images or more broadly as a tool for margin analysis.[9,10] By leveraging elements that are sparse in a given basis, the decomposition algorithm can separate an image into three constituents based on sparsity in the spatial basis, discrete cosine transform (DCT) basis, and curvelet basis.[11] These bases were chosen because they nicely correspond to morphological characteristics; more specifically, nuclei are sparse in the spatial basis, whereas muscle is sparse in the DCT basis and adipose is sparse in the curvelet basis. Thus, through leveraging these sparse elements, our goal is to isolate nuclei in an image and subsequently calculate parameters that can describe the presence or absence of disease. More specifically, when applying the algorithm we let y denote the acquired image and obtain estimates of the tissue components by solving a regularized least squares inverse problem:

$$\left(\hat{x}_{\text{spatial}}, \hat{\theta}_{\text{DCT}}, \hat{\theta}_{\text{curvelet}}\right) = \operatorname*{arg\,min}_{x_{\text{spatial}}, \theta_{\text{DCT}}, \theta_{\text{curvelet}}} \frac{1}{2}\left\|y - (x_{\text{spatial}} + F\theta_{\text{DCT}} + C\theta_{\text{curvelet}})\right\|_2^2$$

$$+ \tau_{\text{spatial}}\left\|x_{\text{spatial}}\right\|_1 + \tau_{\text{DCT}}\left\|\theta_{\text{DCT}}\right\|_1 + \tau_{\text{curvelet}}\left\|\theta_{\text{curvelet}}\right\|_1$$

$$\hat{x}_{\text{DCT}} = F\hat{\theta}_{\text{DCT}}$$

$$\hat{x}_{\text{curvelet}} = C\hat{\theta}_{\text{curvelet}}$$

$$\hat{x}_{\text{approx}} = \hat{x}_{\text{spatial}} + \hat{x}_{\text{DCT}} + \hat{x}_{\text{curvelet}}$$

where the operators F and C represent the inverse DCT and curvelet transform respectively. An example of the power of this algorithm is shown in Figure 1. Essentially, the nuclei can be isolated from the heterogeneous background, which typically contains muscle, captured by the DCT dictionary, and adipose, which is captured by the curvelet dictionary.
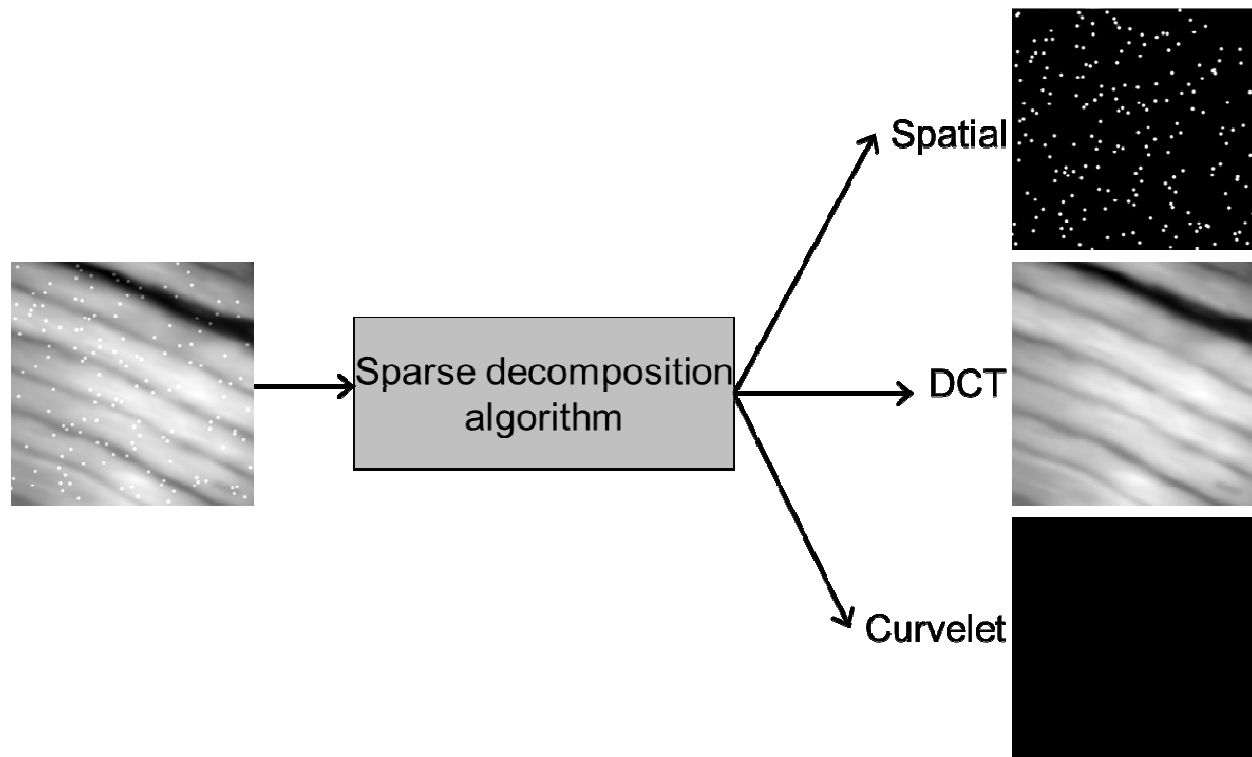
Figure 1: Sparse decomposition illustration. An image containing longitudinal muscle fibers with tumor nuclei scattered throughout can be separated into its constituents through the sparse decomposition algorithm. The spatial image captures the randomly distributed nuclei, while the DCT image describes the periodic muscle components and the curvelet image captures the curved outline of adipose cells. In this example the curvelet image is black because there is no adipose tissue present in the original image.

Once images were decomposed into their constituents, quantitative image parameters were calculated from the resulting segmented images. In order to calculate parameters such as size and density of nuclei, the decomposed spatial images were converted to binary images using Otsu's method, which chooses a threshold to minimize the intraclass variance of the black and white pixels. From the binary images, parameters including the size and density of nuclei, and the distance between nuclei (nearest neighbor calculated through the Euclidean distance transform) were calculated.

Since one of our goals is to isolate cell nuclei in an image and then measure their properties computationally, an appropriate quantitative gold standard was required to validate the approach (in this case, given by the nuclear size calculated from H&E micrographs of the same tissue). H&E micrographs were analyzed by isolating the blue nuclei through converting to the L*a*b color space, applying clustering functions, and converting to binary images. From the binary images, the average size and size distribution of nuclei were calculated and compared to the size of nuclei in the corresponding high resolution image taken from the same tissue site. Scatterplots of these results are shown below in Figure 4.

Results:
First in order to illustrate that our high resolution imaging system can directly recapitulate anatomical features, frozen tissue slices mounted on glass slides were raster-scanned to create mosaics of the tissue face. Because these sections were already mounted on the slides, they could be directly stained with H&E to enable side by side comparison. This comparison is

shown in Figure 2. Purple tumor is seen throughout the left hand side of the H&E micrograph, while pink muscle fibers are present in the right hand side of the section. Similarly, HRME imaging shows a dense collection of disorganized nuclei, characteristic of tumor tissue throughout the left hand side of the panel, while muscle fibers in cross section can be seen throughout the right hand side.
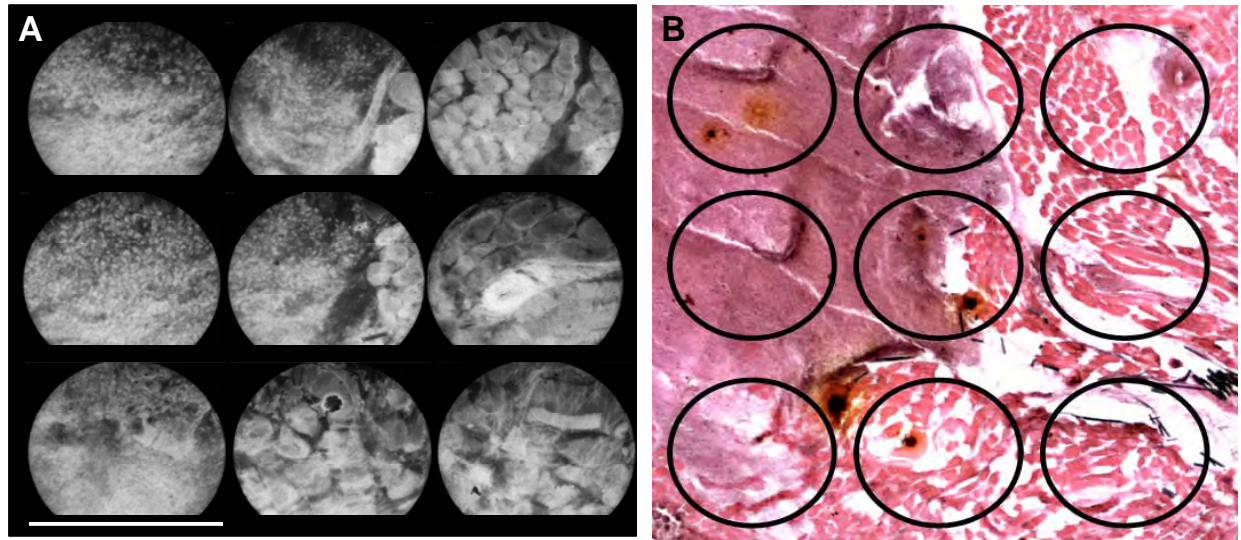

Figure 2: Ex vivo imaging mosaic. Panel A) delineates a tissue section that was raster-scanned to create mosaics of the tissue face. The HRME images in A) can be directly compared to the spatially concordant H&E micrograph shown in B).

Next we applied the sparse decomposition algorithm to segment the panel of images into its constituents. First, the central regions of the images were cropped so as to remove the fiber bundle edge that is present in each individual image (Figure 3A). These cropped images were the input into the sparse decomposition algorithm. The output from sparse decomposition is shown below in Figure 3. More specifically, Figure 3B, C, and D show the spatial, DCT, and curvelet outputs from sparse decomposition respectively. Figure 3B captures the nuclei present in the image, whereas Figure 3C and 3D capture more of the background, which in this example is comprised of muscle fibers in cross section. Most notably, we can see a much denser collection of nuclei in areas that spatially correspond to the presence of tumor tissue, whereas there are much fewer nuclei present in the normal tissue areas. Additionally, we observe that some of the muscle fibers are represented in the curvelet as well as the DCT images—this is due to the fact that muscle fibers in cross section are very similar in size and shape to adipose cells.
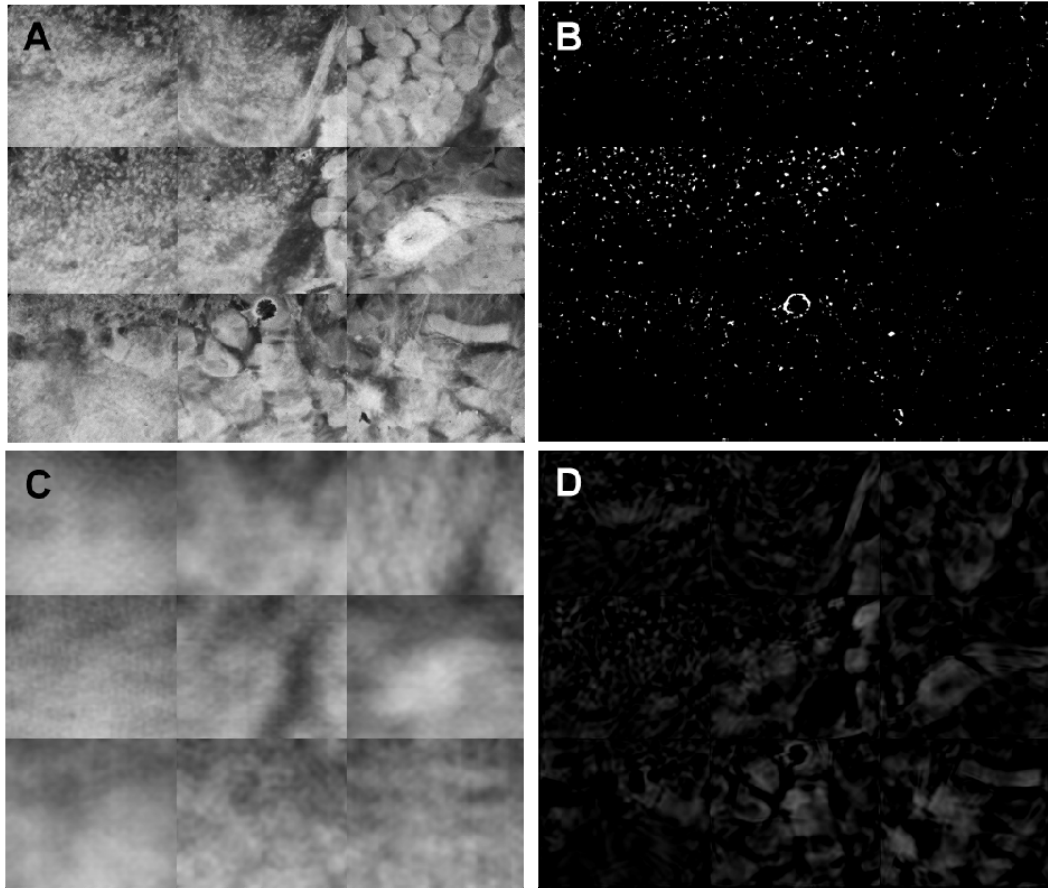
Figure 3: Sparse decomposition applied to the ex vivo mosaic in figure 2. A) shows the original images that have been cropped to remove the fiber bundle rim. B), C), and D) show the spatial, DCT, and curvelet outputs from sparse decomposition respectively. The region containing tumor cells corresponds to more representation in the spatial panel (B), whereas more of the muscle fibers/background is represented in the DCT and curvelet panels (C and D).

Since one of our goals is to isolate cell nuclei in an image and then measure their properties computationally, an appropriate quantitative gold standard was required to validate the approach. H&E micrographs were converted to binary images, and then the density, average size, and distance between nuclei (nearest neighbor or NN) were calculated and compared to the density, size, and NN of nuclei in the corresponding high resolution image taken from the same tissue site. 5 tumor HRME/H&E pairs and 5 tumor + muscle HRME/H&E pairs were included in this analysis. Scatterplots of these results are shown below in Figure 4. Figure 4A shows that sites that contain tumor only have a denser collection of nuclei than sites that contain both tumor + muscle. What is more, this relationship holds not only for the gold standard H&E, but is also directly reflected in our HRME image analysis. We can see a similar trend in Figure 4C. There appears to be a smaller distance between nuclei in tumor only sites than for the tumor + muscle sites. Again this trend is reflected in *both* the H&E micrographs and HRME images. Lastly, we see no trend in nuclear sizes, either with H&E or HRME. This is expected because in both cases we are examining tumor nuclei, which we expect to be approximately the same size across tissue specimens.
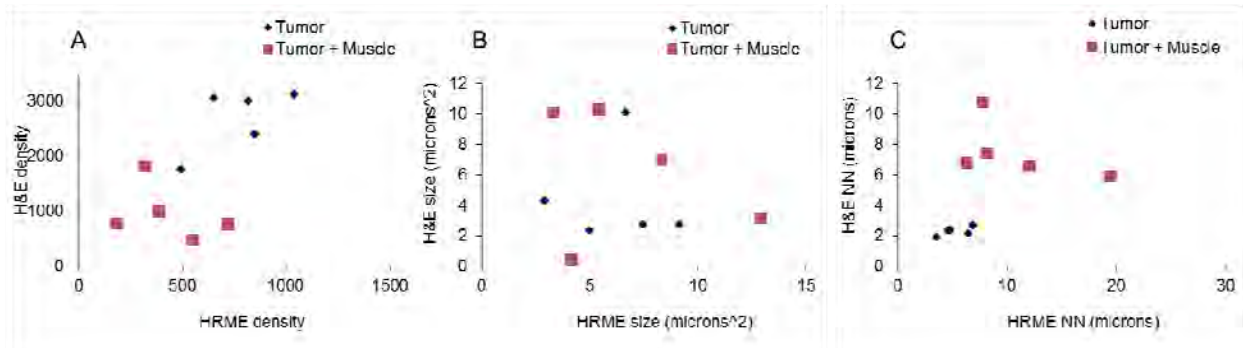
Figure 4: HRME sparse decomposition output compared directly to H&E micrographs. Nuclei were isolated through sparse decomposition and then their density, median size, and average distance in between (nearest neighbor or NN) were calculated. The same set of parameters was calculated from the corresponding H&E micrographs. Trends for density, size, and NN are shown in A), B), and C) respectively.

2) *Ex vivo* clinical mastectomy study

Methods:

As mentioned previously, we also applied our image analysis techniques to a cohort of HRME images captured from clinical mastectomy specimens. Mastectomy specimens were used in order to enable us to more quickly assemble a "library" of both malignant and benign representative high resolution fluorescence images. Ultimately, having a library of images that contains the breadth of normal tissue variants as well as malignant variants enables us to more appropriately evaluate the potential of our analytical imaging approach.

Imaging protocol: For this pilot study, patients undergoing a mastectomy were consented. Immediately after the breast was removed from the patient, the collaborating pathologist inked the deep margin of the breast, and then bisected the tissue with a knife to expose the tumor inside the breast. To be clear, no ink was present on the tumor or normal tissue on the inner surface of the cut tissue. Once the tumor was bisected, 0.01% (w/v) acriflavine (Sigma-Aldrich) dissolved in phosphate buffered saline (PBS) was applied topically to regions within the bisection (tumor) and to fatty regions surrounding the bisection (normal tissue). The distal end of the HRME fiber bundle was placed in contact with the tissue and images were acquired. Between each probe placement the distal end of the probe was cleaned with 55% ethanol.

Pathologic co-registration: During the imaging session specific sites of interest were inked with 1 mm dots for pathologic co-registration. After imaging and inking was complete, the tissue was returned for standard pathologic processing, and the resulting hematoxylin and eosin (H&E) stained slides were reviewed by an expert oncology pathologist who was blinded to the results of HRME imaging. For each inked area a diagnosis was given.

Results:
Seventeen patients were consented for this study. A break down of the pathology confirmed sites stratified by tissue type is shown in

Table 2. Normal tissue variants include adipose, fibroadipose, fibroglandular, fibrous, and fat necrosis. Malignant tissue variants include invasive ductal carcinoma (IDC), invasive lobular carcinoma (ILC), and mucinous carcinoma.

Table 2: Pathology confirmed sites

Tissue type	Count
Adipose	17
Fibroadipose	12
Fibroglandular	5
Fibrous	19
Fat necrosis	5
IDC	5
ILD	2
Mucinous	1
Total	66

A panel of normal tissue variants can be seen in Figure 5. Each row corresponds to a different tissue type, while each column corresponds to the input and outputs from the sparse decomposition algorithm. Column 1 contains the original image that has been cropped to remove the fiber bundle rim. Column 2 contains the approximation of the image, which is the sum of the spatial image (column 3), DCT image (column 4), and curvelet image (column 5). As seen, the spatial column picks up the nuclei that are associated with either the adipose cells or fibrous components of the tissue, while the DCT column picks up the stringy fibrous structures, and the curvelet column picks up the curved outline of adipose cells.
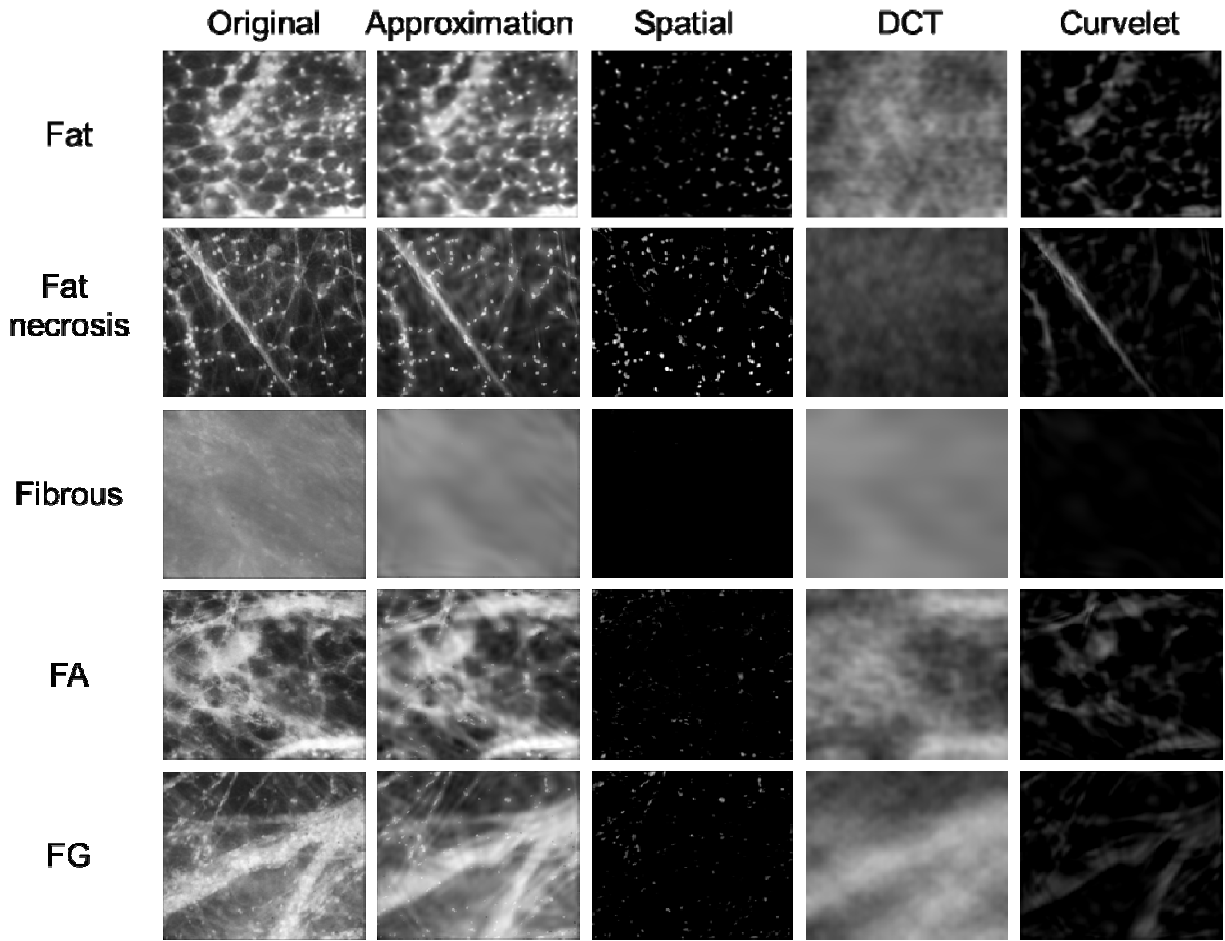
Figure 5: Sparse decomposition applied to representative clinical breast images of normal tissue. The original image was cropped to remove the fiber bundle (column 1). The outputs from sparse decomposition are shown in columns 2 through 5. Column 2 contains the approximation of the image, which is the sum of the spatial image (column 3), DCT image (column 4), and curvelet image (column 5).

A panel of malignant tissue variants can be seen in Figure 6. As seen, the spatial column picks up many of the nuclei present in the original image, while there is very little structure picked up in the DCT or curvelet columns. This is expected because the main feature of malignant tissue is the disorganized collection of dense nuclei.
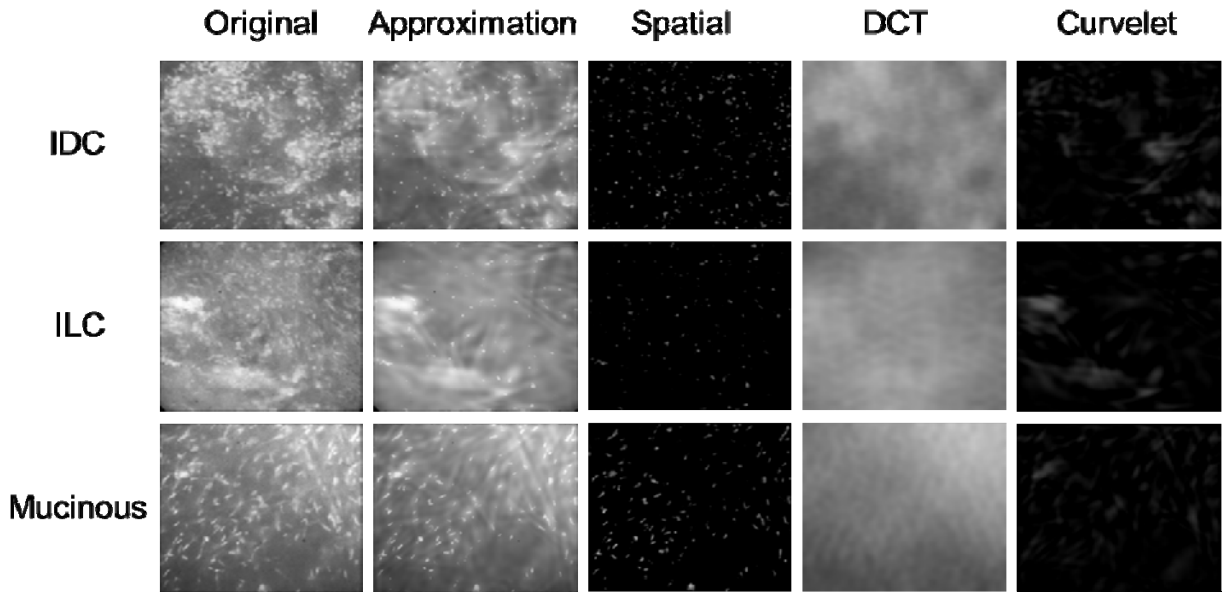
Figure 6: Sparse decomposition applied to representative clinical breast images of malignant tissue. The original image was cropped to remove the fiber bundle (column 1). The outputs from sparse decomposition are shown in columns 2 through 5. Column 2 contains the approximation of the image, which is the sum of the spatial image (column 3), DCT image (column 4), and curvelet image (column 5).

Through validating the image analysis on murine sarcoma specimens and through applying the algorithm to mastectomy samples, we feel confident in moving forward to start the 200 patient lumpectomy study. As discussed in the original document (and above), we plan to acquire data with both the spectral imaging platform and the HRME on the same clinical lumpectomy specimen to determine if we can improve our detection accuracy through harnessing the advantages of each approach.

Plans for year 3:
Plans for year 3 include fine tuning this algorithm for clinical breast specimens, identifying endpoints/parameters that have diagnostic potential (such as the density of nuclei in the spatial images), and building predictive models that can quantitatively diagnose high resolution images in real time.

Spectral imaging component: Wide-field Quantitative Diffuse Reflectance Imaging of breast tumor margins

Introduction
The second aspect of our proposed work in Aim 1 is to conduct a prospective validation study of our previously developed wide-field, quantitative diffuse reflectance imaging device, for detecting residual carcinoma at the margins of resected partial mastectomy specimens. In Year 1, we have been preparing for this study in 2 primary areas: 1) technology refinement, and 2) algorithm development. In Year 2, we have 1) continued algorithm development, 2) clinical data collection with refined technology.

1.   Algorithm Development: *Effects of Patient Demographics on Optical Properties*
Introduction: In addition to the high resolution fluorescence imaging, we have been refining our wide-field spectral imaging approach. In last years report we discussed in detail our methodology for acquiring wide-field spectral images with the 8CH probe, how the data from that study was analyzed in over 100 patients, and discussed the use of a conditional inference tree model to predict surgical margin status. We also had initial data that suggested that patient demographics could impact the accuracy of predictive models for margin diagnosis. Since then we have further investigated the impact of patient demographics (specifically radiographic breast density and neoadjuvant chemotherapy status) on the optical properties of normal tissue and how these changes impact optical contrast and the accuracy of the conditional inference tree model. These results are described in more detail below.

Methods:
Details of the analysis of the diffuse reflectance data from the partial mastectomy specimens can be found in prior publications[13-16] and were discussed in previous reports. Briefly, spectra were corrected for daily variations in optical throughput using a Spectralon reflectance standard, and were normalized by the CCD integration time. An inverse Monte Carlo model[13,17-19] was used to obtain values for THb concentration, β-carotene concentration and the wavelength-averaged reduced scattering coefficient from 450-600 nm ($<\mu_s'>$), for each measured site (or pixel) on the specimen surface. Using all pixels from the lumpectomy specimens, empirical cumulative distribution functions (eCDFs) were created and separated by various patient demographics. We found that the demographics that impact the optical data most are radiographic breast density and neoadjuvant chemotherapy status. Therefore, the eCDFs were separated by breast density and neoadjuvant status. Each patient is assigned a value for radiographic breast density based on a mammogram: 1 (fatty), 2 (scattered fibrous), 3 (heterogeneously dense), or 4 (extremely dense). For the analyses in this paper a score of 1 or 2 was considered to be low density, while a score of 3 or 4 was considered to be high density. Patients who received chemotherapy prior to surgery were considered "neoadjuvant-chemo" cases and patients who did not receive any prior therapy (chemotherapy, endocrine, or radiation) were considered to be "neoadjuvant naïve". To calculate statistical differences between the eCDFs, empirical p-values for a Kolmogorov-Smirnov statistic were computed using blocked permutation to maintain the correlation structure of multiple site level measurements within each margin.

The conditional inference tree described in our previous report is compared to new models which take into account breast density and neoadjuvant therapy status (both chemotherapy and endocrine therapy). The sensitivity, specificity, and classification accuracy of the wide-field spectral images are also compared to the performance of the surgeon at detecting residual cancer on the primary specimen that is excised.

Results:
Our previous spectroscopy studies[16] have shown that the local microenvironment of the breast greatly affects the optical signatures of both benign and malignant sites. The composition of the human breast is highly variable from person to person; although the organ is composed of the same tissue types, the specific arrangements and relative contributions of these tissue types are patient specific. In addition, it is well known that the composition of breast tissue can change significantly within a woman as a function of factors such as the menstrual cycle, pregnancy, lactation, menopausal status, body weight, and age. In order to identify optical parameters which may be robust predictors of margin status in patients of varying demographics, it is important to understand how these optical parameters are modulated by normal changes in breast composition. Therefore, we have been investigating how patient characteristics affect

the absorption (THb and β-carotene) and scattering of pathologically negative surgical margins (benign tissue) and how this affects the ability to differentiate negative from close/positive surgical margins. We have found that there are 2 patient demographics that have the greatest impact on our optical data; the first is radiographic breast density and the second is neoadjuvant therapy status.

For the analysis of the breast density data; 92 margins were measured in 72 neoadjuvant naïve patients. Figure 7 (below) shows eCDFs of every measured site on the negative surgical margins (n=46), separated by radiographic breast density.

Table 3 shows the statistics for the differences between the eCDFs for each optical parameter. These plots show that β-carotene was significantly higher in the margins of high density patients which we believe is due to differences in adipocyte size. In an initial analysis of histological images (n=20) of adipocytes we found that there were 197±51 cells in low density images and 250±60 cells in high density images (p=0.041). This indicates that the cells are larger in low density patients and could be the reason why we saw increased levels of β-carotene in the high density patients. THb and $<\mu_s'>$ were also higher in the high density patients (although not significant) which was likely due more fibro-glandular tissue and an increase in vessels.

Figure 7: Empirical cumulative distribution functions of all measured sites from pathologically negative, neoadjuvant naïve margins. Data is separated by radiographic breast density.

Table 3: P-values calculated using modified Kolmogorov-Smirnov tests for the differences between CDF's from negative margins.

THb (μM)	0.083
β-carotene (μM)	0.022
$<\mu_s'>$ (cm^{-1})	0.60

For the analysis of the neoadjuvant data; 129 margins were measured (92 neoadjuvant naïve plus an additional 37 neoadjuvant margins). Figure 8 (below) shows eCDFs of every measured site on the negative surgical margins, separated by neoadjuvant status.

Table 4 shows the statistics for the differences between the eCDFs for each optical parameter. Chemotherapy can induce fibrosis so it is not surprising that we found a significant increase in $<\mu_s'>$ in the negative margins of patients who had undergone chemotherapy prior to surgery. Although not significant, we found that THb and β-carotene were lower in patients who had neoadjuvant chemotherapy.
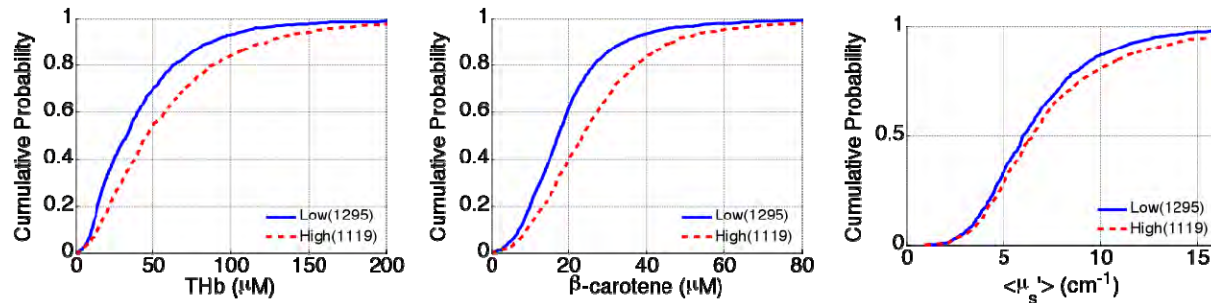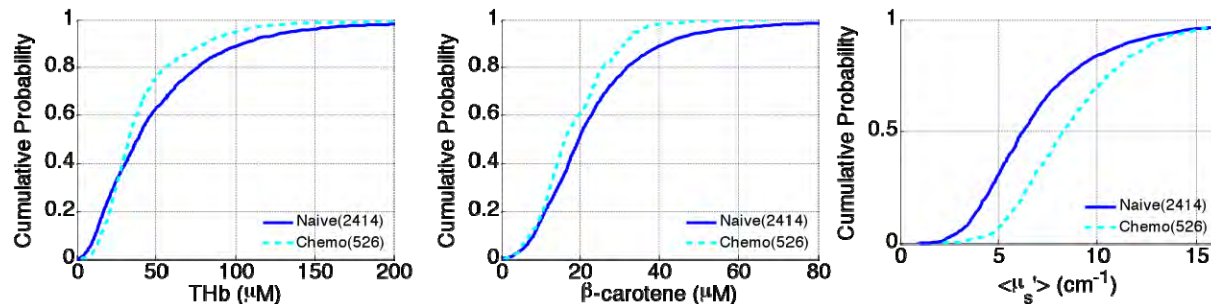
Figure 8: Empirical cumulative distribution function of all measured sites from histologically negative margins. Data is separated by neoadjuvant status. Patients who didn't receive any neoadjuvant therapy are considered "naïve" versus those who received chemotherapy (chemo).

Table 4: P-values calculated using modified Kolmogorov-Smirnov tests for the differences between CDF's from negative margins.

THb (µM)	0.31
β-carotene (µM)	0.43
$<\mu_s'>$ (cm^{-1})	0.0067

In last years report we showed the classification results from a CIT model based on the 92 margin (72 patient) dataset. Since then we have found that both radiographic breast density and chemotherapy impact the optical properties of benign tissue. Therefore, it should not be surprising that the contrast between negative and positive margins is also affected. In Table 5 we show the classification results of the original CIT model (non-mammographic breast density specific) with the margins separated by low and high density. These results show that the model is better at predicting margin status in the high density patients; due to the differences in the benign tissue of the different types of patients. Since the optical parameters are affected by breast density, we developed a classification model for each group of patients. All patients will have undergone a mammogram prior to surgery; therefore, breast density will be known prior to the measurement process and could be used *a priori* in a statistical model. Table 5 shows the results when a model is built with breast density known *a priori* (mammographic breast density specific). These results also show that surgical margin status is better predicted in the high density patients. It also shows that the accuracy is better when breast density is known ahead of time. In addition, this table contains the surgeon's performance based on the primary specimens. These numbers do not reflect the surgeons' true performance because it does not account for additional shavings of tissue that were taken during the first operation. For our measurements we only measure the primary specimen, therefore, we compare the surgeons' performance on the same specimens. Compared to the surgeons' performance, the optical device shows an increase in sensitivity, specificity, and accuracy. The results also show that the surgeon has a more difficult time identifying positive margins in high density patients (lower accuracy). The optical device would be beneficial for this patient population.

Table 5: Diagnostic results of the prediction classification of the CIT model separated by radiographic breast density. The first model does not account for breast density. The second model uses breast density as a priori data. The surgeon's performance is based on the primary specimen and no additional shavings taken during the first operation.

	Sensitivity	Specificity	PPV	NPV	Accuracy
Non-mammographic breast density specific CIT model					
Low	83	64	68	80	73
High	87	67	74	82	77
Mammographic breast density specific CIT models					
Low	78	76	74	79	77
High	74	90	89	76	82
Surgeon					
Low	70	28	47	50	48
High	61	24	47	36	43

In the eCDFs above we showed that in addition to radiographic breast density, chemotherapy also affects the optical parameters of benign tissue. A CIT model based on a dataset of 129 margins (neoadjuvant and neoadjuvant naïve patients) was built without considering breast density or neoadjuvant status *a priori*. A second model was built with breast density and neoadjuvant status as priors. Table 6 shows the results of these two models. Knowing breast density and neoadjuvant status prior to surgery increased the sensitivity, specificity, and accuracy of margin classification.

Table 6: Diagnostic results of the prediction classification of the CIT model when breast density and neoadjuvant status are unknown and known a priori. The first model does not account for breast density or neoadjuvant status. The second model uses breast density and neoadjuvant status as a priori data.

Sensitivity	Specificity	PPV	NPV	Accuracy
Non-breast density and non-neoadjuvant specific CIT model				
63	74	70	68	69
Breast density and neoadjuvant specific CIT models				
70	83	80	74	77

2.   Clinical Data Collection with Refined Technology

Introduction:
We have completed the development of the 49-channel imaging device which allows for faster acquisition of wide-field spectral images. A schematic of the device is shown in Figure 8. In year 2, we have begun recruiting patients undergoing both partial mastectomy and reduction mammoplasty for the imaging protocol. The goal of this imaging protocol is to use wide field spectral imaging of the entire margin followed by high resolution fluorescence interrogation of optically identified suspicious sites.

Figure 9. A 49-channel optical spectral imaging system: (A) arrangement of collection fibers to be imaged onto the CCD, (B) arrangement of illumination fibers in the illumination adaptor, (C) layout of the common end, and (D) imaging probe tip cover made up of a plexi glass plate with a thin film layer to create a barrier with the imaging probe tip and the specimen.

Methods:
The custom 49-channel fiber optic imaging array was fabricated and the custom software package was implemented. The hardware for the 49-channel system was assembled and tested. In May 2011, the probe was tested and characterized using tissue mimicking phantoms prior to clinical use. Prior to clinical implementation, we used the 1st generation, 8-channel device combined with high resolution fluorescence imaging to begin initial testing. We were able to use both devices to measure 7 patients (margins) with 35 pathologically confirmed sites. Once the 49-channel system became clinically viable, we measured a total of 16 patients with this device. Starting in July 2011, patients undergoing partial mastectomy (lumpectomy) or reduction mammoplasty surgery were recruited for this study. Given the time restraints for using our devices in the operating room, for some procedures we have only been able to use one device, either the high resolution fluorescence imaging device or the spectral imaging device. The specimen was oriented in a custom made specimen box and a wide-field spectral

image of a tumor margin was acquired. The wavelength-dependent spectral data was analyzed using the inverse Monte Carlo Algorithm producing parameter maps of total hemoglobin, β-carotene, and scattering. From these parameter maps, "hot spots" were identified and then interrogated with the high resolution fluorescence imaging probe. These "hot spots" were then inked to obtain histopathology of these suspicious sites. Due to IRB protocol constraints, we were not able to obtain histopathology on the mammoplasty samples. We have been able to image 16 full margins with 66 pathologically confirmed sites. Due to time constraints in the OR, we were only able to interrogate "hot spots" on 5 margins resulting in 17 pathologically confirmed sites.

Results:
Hemoglobin (H0267 Ferrous Hemoglobin, Sigma-Aldrich) and 1.025µm diameter polystyrene spheres (Polysciences) diluted with distilled water were used to construct 12 tissue mimicking phantoms. The inverse Monte Carlo model was used to extract the scattering (μ_s') and absorption (μ_a) coefficients from the phantoms using each phantom as a reference to extract the optical properties of all 12 phantoms. The mean optical properties (420-630 nm) for these phantoms are shown in

Table **7** and resulted in an average μ_s' error of 3.57 ± 1.06% and an average μ_a error of 8.72 ± 6.93% over all 49 channels and all reference/target phantom combinations.

Table 7: Mean optical properties of the tissue mimicking phantoms from 420-630nm.

Phantom	$<\mu_s'>$ (cm^{-1})	$<\mu_a>$(cm^{-1})
1	9.96	0.30
2	9.54	0.57
3	9.15	0.82
4	8.79	1.05
5	8.46	1.27
6	8.15	1.46
7	7.86	1.65
8	7.60	1.82
9	7.35	1.98
10	7.11	2.13
11	6.90	2.27
12	6.69	2.40

The breakdown of margin status and site diagnosis for each of the devices used to date is shown in Table 8. We are still optimizing reference phantoms to extract the most accurate parameter maps, but demonstrate an example margin image and corresponding high resolution images in Figure 10.

Table 8: Margin status and pathologically confirmed site diagnosis for 1st and 2nd generation devices used in combination with high resolution fluorescence imaging.

	8-channel	49-channel	Total
Margin Status			
Positive	2	0	2
Close	2	4	6
Negative	3	11	15
Mammoplasty	0	1	1
Total Margins	7	16	23
Site Diagnosis			
IDC	2	2	4
DCIS	0	0	0
Adipose	25	32	57
Fibro-adipose	1	14	15
Fibro-glandular	1	1	2
Mixed/Other	6	17	23
Total Sites	35	66	101

Of the sites shown in Table 8, we obtained high resolution images for all of the 8-channel device measurements, but only 17 of the sites with the 49-channel device. These sites were comprised of 5 adipose sites, 4 fibro-adipose sites, 7 mixed sites, and 1 IDC site.
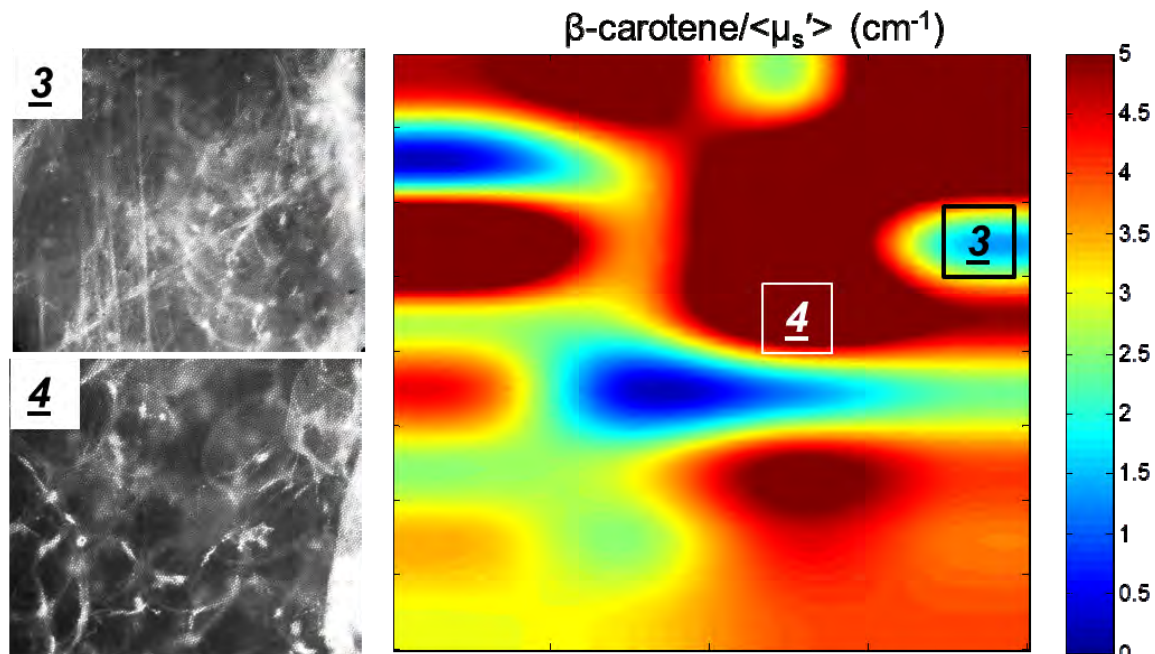
Figure 10: A map of β-carotene/$<\mu_s'>$ (cm^{-1}) from a close margin. Sites 3 & 4 were interrogated with the high resolution fluorescence imaging system and inked for histopathology. Both sites were diagnosed as adipose tissue but it is evident that site 3 has more fibrous tissue in the high resolution image which corresponds to increased scattering and a decreased ratio.

Conclusions:
In year 2, we have completed the implementation of the 49-channel device resulting in a clinically viable system. We demonstrated that this system could accurately extract optical properties through tissue mimicking phantom studies. We encountered a delay in clinical implementation of the 49-channel system, so we took the initiative and began testing and analyzing the protocol using the 8-channel system. Lastly, we were able to use the 49-channel device to image 16 patients in an intraoperative setting followed by high resolution fluorescence imaging of sites. Initial analysis shows potential for using high resolution imaging to further understand the underlying morphology and lead to improved margin assessment.

Plans for year 3:
In year 3, we will continue recruiting patients for the imaging protocol and will determine if the high resolution device enhances that ability to detect surgical margin status at time of surgery. We have amended our protocol to allow us to obtain pathology from mammoplasty specimens in order to fully understand the spectral and morphological contrast associated with all tissue types.

Aim 2: Optical quantitative biology of different breast cancer subtypes.

Introduction:
The objective of the work in Aim 2 is to use optical spectroscopy to measure optical markers of the tumor microenvironment that are morphologically based (with HRME) and functionally based (with spectroscopy) in women with cancers representing a wide variety of molecular subtypes, and to determine whether these optical measures can be predictive of eventual chemotherapy response in a subset of the patients who are measured prior to commencement of chemotherapy. In Year 2, we have completed a feasibility study using HRME to capture morphologically based information from biopsy specimens. In addition, we started developing and building an integrated probe to simultaneously measure high resolution micro-endoscopic fluorescence images and corresponding diffuse reflectance spectral measurements.

1. HRME biopsy study

Introduction:
The ability to predict response to therapy would be an invaluable tool to the medical community. However, in order to be adapted into clinical practice, it is necessary that technological development be compatible with current medical paradigms. A critical point in the clinical management of breast cancer is the initial biopsy that is taken prior to administering therapy, such as chemotherapy. If an additional research biopsy could be acquired at this point, measured and analyzed appropriately, it could be used to predict response to therapy and improve overall patient care and management. Towards this end, we have begun to assess the potential of using the high resolution microendoscope (HRME) described in detail in Aim 1 to measure clinical biopsy specimens in real time.

Moving forward we have identified two different ways in which high resolution imaging and analysis could be used clinically. The first is that HRME imaging could identify if a biopsy is positive or negative during the biopsy procedure. Thus, if assessing the response to chemotherapy is dependent upon acquiring a positive biopsy (so that the cancer can be appropriately diagnosed and any malignant markers associated with the cancer can be

identified), then HRME imaging could be used to ensure that a positive biopsy is acquired during the procedure. The second way in which HRME imaging of biopsy specimens could be used clinically is to potentially predict the response to chemotherapy itself. For example, there could be an anatomical signature, such as the orientation of collagen surrounding the malignant lesion that may be predictive of a response to therapy. In particular, other groups have identified tumor associated collagen signatures (TACS) that have been shown to be predictive of patient outcome and survival.[12] Moving forward, we plan to assess the potential of both of these clinical applications through the measurement of ex-vivo biopsy samples. Additionally, we are developing a probe that integrates HRME imaging with spectral measurements, allowing us to simultaneously acquire structural and physiological information. This integrated device will allow us to examine how HRME information is related to spectral endpoints and how the combination can contribute to a better identification of the tissue. We have completed the assembly of the probe and are moving forward with instrument characterization and measurements of ex-vivo clinical specimens.

Methods:
Imaging protocol: For our pilot biopsy study, patients undergoing a biopsy procedure were consented. After the biopsy was removed from the patient, 0.01% (w/v) acriflavine (Sigma-Aldrich) dissolved in phosphate buffered saline (PBS) was applied topically to the surface of the specimen. The distal end of the HRME fiber bundle was placed in contact with the tissue and images were acquired. The biopsy was scanned length-wise by systematically moving the probe in 1 mm increments over the tissue surface. Once one side was scanned, the biopsy was rotated 180 degrees and the length-wise scanning process was repeated. In order to improve the accuracy and reproducibility of these movements the fiber bundle was secured in a custom probe holder fiber chuck which was mounted on an x-y translation stage. Between each probe placement the distal end of the probe was cleaned with 55% ethanol.

Pathologic co-registration: After the imaging session the surface of the specimen was inked for pathologic co-registration. In order to maintain the proper orientation of the specimen for pathological evaluation, each end was inked with a different color. After imaging and inking was complete, the tissue was returned for standard pathologic processing, and the resulting hematoxylin and eosin (H&E) stained slides were reviewed by an expert oncology pathologist who was blinded to the results of HRME imaging. A diagnosis for each end of the biopsy as well as a diagnosis for the middle portion of the biopsy was given.

Results:
Five patients were consented in this study. Table 9 shows the tissue types that were identified in each biopsy (whether from the diagnosis at each end or from the middle). Each number represents the number of biopsy cases in which that tissue type was identified out of the 5 total biopsy specimens that were measured for this pilot study. For example, in the five biopsy cases measured thus far, 3 of them have contained fibro-adipose tissue.

Table 9. Pathological diagnosis of 5 biopsy specimens.

Tissue type	Count
Fibroadipose	3/5
Fibrous	4/5
DCIS	1/5
IDC	4/5
ILC	1/5

Figure 11 shows an example of one of the biopsies from this initial cohort. As described in the methods each side was scanned length-wise. In this example, the left hand side was inked green and the right hand side was inked orange. The pathological diagnosis for the green tip—middle—orange tip is shown below the specimen. As seen, large round cells and with string-like fibrous tissue, characteristic of fibro-adipose tissue, can be seen on the left hand side, while the rest of the panel is filled with a random distribution of disorganized nuclei, which is characteristic of IDC.

FA + DCIS ⟶ IDC + fat ⟶ IDC
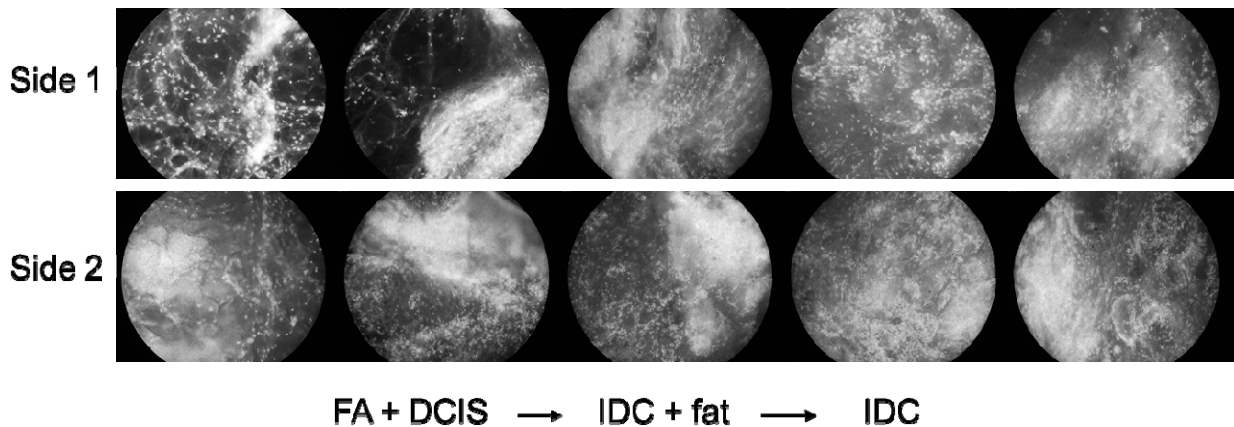
Figure 11: Representative HRME imaging of a biopsy specimen. Both sides of the biopsy we scanned length-wise. Sides are labeled as side 1 and side 2. A pathological diagnosis was given for the left end, middle, and right end respectively.

Plans for year 3:
Plans for year 3 include increasing enrollment in the biopsy study, applying image analysis techniques described in Aim 1 to diagnose HRME images during biopsy procedures, looking for correlations between image features/endpoints and response to therapy, and characterizing and clinically implementing the integrated probe. In collaboration with Rice University, we will explore the correlation between morphologic biomarkers assessed from high resolution optical images (epithelial cell density and N/C ratio; collagen density, fiber size, fiber linearity; adipocyte size and density) and histologic diagnosis and biomarkers of cancer risk and progression, define metrics of breast density which can be calculated from high resolution optical images of breast tissue and correlate with histologic diagnosis, biomarkers of cancer risk and progression and explore correlations between microscopic definitions of breast density developed above with macroscopic-scale metrics of breast density.

In addition to the data presented above, Rice University previously acquired images from resected tumor and needle biopsy specimens in 24 patients. Images were obtained using both a

commercial laser scanning confocal device and the HRME described in the original proposal. The commercial confocal system allows for complete mapping of tissue specimens and direct site comparison with histological sections. These images have been assembled into a library of normal, non-neoplastic features and neoplastic lesions to facilitate comparison between high resolution optical images and the corresponding histological sections. This library will be used as part of the analyses to be carried out in the next year.

SD separation: 250-1000um
Sensing depth ~ 2mm
800um
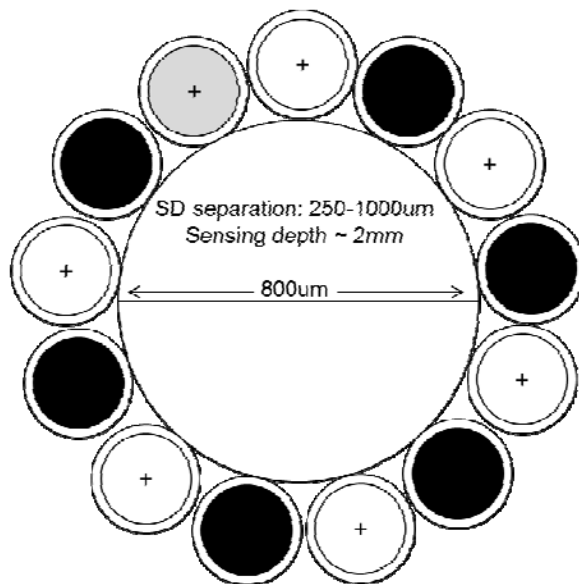
Figure 12: Fiber geometry for the integrated probe. White fibers are illumination fibers; black fibers indicate collection fibers. Gray indicates a dead fiber. All fibers are 200µm in diameter. The core HRME fiber bundle is about 800µm in diameter. The source to detector separations range from 250-1000µm with a maximum sensing depth around 2mm.

Lastly, we were able to build an integrated probe that incorporated the capabilities of both HRME and spectroscopy into one system. A schematic is shown in Figure 12. The protocol used will be similar to previous studies: taking measurements and inking for pathology. This integrated device will allow us to examine the relationships between diffuse reflectance spectra, HRME images, and histological information from all specimen types. Ultimately, we can use this technology to better understand the combined and independent capabilities of HRME and spectroscopy. Moving forward, we will perform characterization studies of the new integrated device and begin measuring clinical specimens.

Aim 3: *Optical quantitative biology to assess therapy response in different sub-types of breast cancer:*

As stated in our report for Year 1, the research goals for aim 3 have altered slightly from the original statement of work. As proposed, murine window chambers have been implemented for the intra-vital monitoring of hemoglobin saturation. In addition, we have started to explore the possibility of using fluorescent glucose analogs to measure glucose uptake in tumors. Toward this end, we and other research groups have demonstrated the ability of 2-NBDG, an optical analog of glucose, to monitor or track changes in glycolysis. We have started to use a murine mammary carcinoma model (4T1) that constitutively expresses red fluorescence protein (RFP).

We will initially measure HbSat and 2-NBDG uptake in response to specific microenvironmental stresses such as chronic and intermittent hypoxia. In the second phase of this study we will use such microenvironmental stresses to modulate the response to chemo- and radiotherapy and determine the feasibility of HbSat and 2-NBDG uptake to predict long-term response to therapy.

Introduction:
In addition to measuring hemoglobin saturation, which can be indicative of tumor hypoxia, another physiological endpoint that we have been interested in measuring is tumor metabolism. Hypoxia has long been associated with poor prognosis in cancer patients. Because hypoxia can also determine the metabolic status or pathway chosen by a cancer cell, it is important to identify whether hypoxia causes certain changes in metabolism that provides a favorable environment for cancer cells to proliferate and metastasize. We are interested in exploring the effects of chronic and intermittent hypoxia on the metabolic response of cancer cells and tumors. The form of hypoxia experienced by a cancer cell depends on its proximity to a food source, i.e. vasculature; cells closer to a blood vessel tend to be exposed to fluctuations in red cell flux due to new and tortuous vessels whereas cells present at the oxygen diffusion limit and beyond tend to be chronically hypoxic.

Our goal is to determine specific changes in the functional and metabolic response of tumors to different forms of stress or hypoxia. Our long-term goal is to identify whether such endpoints could be used to predict long-term tumor behavior. The results from these studies will help guide Aims 3b and 3c.

Methods:
Cell line and animal model: 4T1-RFP cells were implanted in murine window chambers and allowed to grow for 6-7 days. Tumor-bearing mice were divided into 4 groups and exposed to different conditions: 1) alternating cycles of regular air (21% oxygen) and hypoxia (10% oxygen), 2) chronic hypoxia for 3 hours and 3) Regular room air for 6 hours. Normal mice (no cells implanted) were used as controls. We had control animals for each tumor group. Each group had 2-3 mice. All mice were fasted for a period of 6 hours (overlaps with treatment mentioned above) prior to measurement to ensure minimal glucose competition. 100 µl of 6 mM 2-NBDG was injected through the tail vein of the mouse.

Image acquisition and processing: We acquired images of 2-NBDG fluorescence at 525 nm every 300 ms for at least 80 minutes. We used a hyperspectral microscope for acquiring white light transmittance, 2-NBDG fluorescence and RFP fluorescence. Using previously validated algorithms we can process the white transmittance to create maps of hemoglobin saturation in the blood vessels. We selected specific regions in the images that correspond to tumor and non-tumor areas for viewing 2-NBDG fluorescence as a function of time. In addition, we also measured 2-NBDG fluorescence using a confocal microscope to identify the time point of 2-NBDG uptake into the cells.

Results:
Using confocal microscopy, we measured the 2-NBDG uptake in a tumor exposed to regular air. Our results indicate good co-registration between 2-NBDG and RFP fluorescence around 40 minutes post-injection. This is important to know because processing images at peak 2-NBDG fluorescence can be misleading.
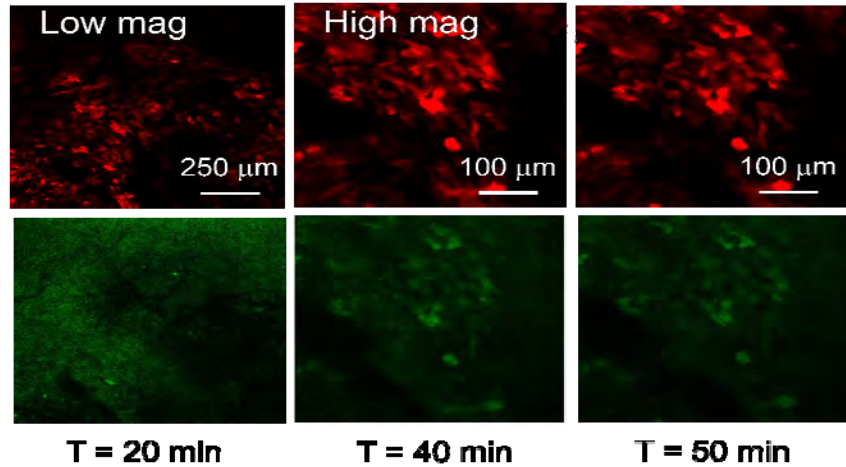
Figure 13. Confocal images of the skin flap window chamber at different time points. Row 1 shows RFP fluorescence from the tumor. Row 2 shows 2-NBDG fluorescence. Images show good co-registration between RFP and 2-NBDG around the 40-minute mark.

We used the hyperspectral microscope to image HbSat, RFP and 2-NBDG fluorescence. Our results indicate that exposure to chronic and cycling hypoxia cause a significant increase in glucose uptake compared to tumors exposed to regular air. In addition, we observed an increase in HbSat in tumors subject to chronic hypoxia compared to tumors exposed to cycling hypoxia or normoxia. Figure 14 shows representative RFP, 2-NBDG and HbSat images from each tumor group.
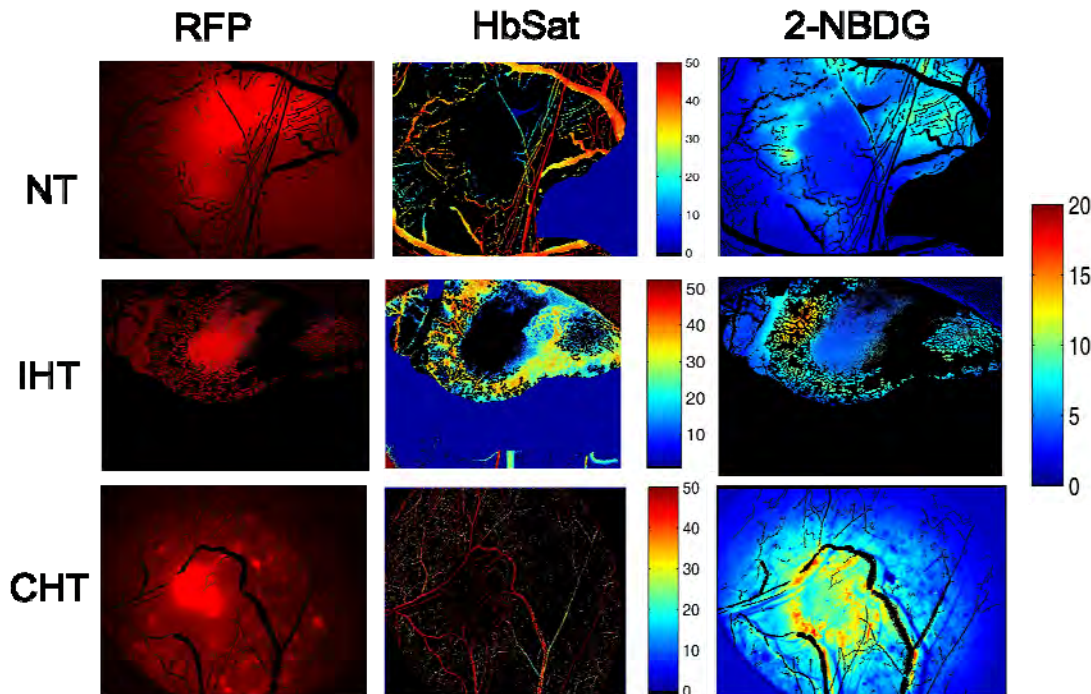

Figure 14. Representative images from each tumor group. Column 1 represents RFP fluorescence and indicates tumor position. HbSat is processed from the white light transmittance and is on an absolute scale. 2-NBDG fluorescence shown here was measured at 5 minutes. NT – normoxic tumor, IHT – intermittent hypoxia, CHT – chronic hypoxia.

Because we measure 2-NBDG uptake over 80 minutes, we can get snapshots of glucose uptake over time. We intend to measure HbSat longitudinally immediately after hypoxic treatment. This can provide information to separate perfusion versus demand-related glucose uptake. In Figure 15, we present the average HbSat in vasculature as well as 2-NBDG uptake at 40 minutes. Note that the selection of the 40-minute timepoint is based on the data presented in Figure 13. Our goal is to examine the same plot over time and determine any correlations with HbSat. Studying the spatial relationships between the two parameters, in response to stress, as a function of time could possibly capture important trends that can help predict long-term tumor behavior.
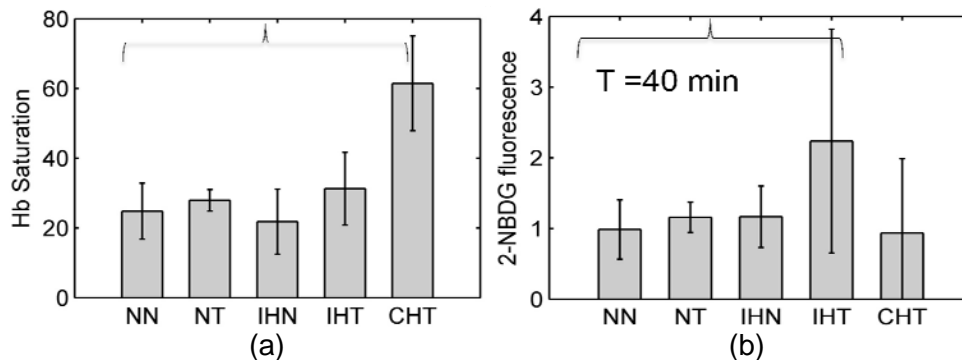

(a)   (b)

Figure 15. (a) Mean HbSat measured in each cohort of animals. (b) Mean 2-NBDG fluorescence. The intermittent hypoxia tumor group had a statistically significant increase in 2-NBDG uptake compared to control (p < 0.05) Chronic hypoxia tumor group had a significantly higher HbSat compared to the other groups. NN – normoxic control, NT – normoxic tumor, IHN – intermittent hypoxia control, IHT – intermittent hypoxia tumor, CHT – chronic hypoxia tumor.

Plans for year 3:
In year 3, our first goal is to complete the ongoing studies in window chamber models and publish our work. We intend to examine the relationship between functional and metabolic tumor response to stress in related cell models: sibling cell lines that are metastatic and non-metastatic, responsive to therapy or non-responsive to therapy. For example, the 4T1 cell line used in our current study has a sibling cell line, 4T07 that is non-metastatic. The 4T1, on the other hand, is highly metastatic (lungs). Determining the response of each of these tumors to stress can help determine if a specific metabolic change is indicative or provides an advantage to tumors. We also plan to extend the quantitative analysis of the data to examine the kinetics of glucose uptake into cancer cells. Specifically, we intend to use compartment models to identify differences in glucose uptake by cells in response to stress.

We have also initiated preliminary efforts to use optical spectroscopy to measure glucose uptake in flank tumors implanted in mice. We already possess validated algorithms that can quantify vascular oxygen saturation measured with optical spectroscopy. Our efforts in Year 3 will be focused on developing and validating algorithms to quantify the 2-NBDG fluorescence measured from the tumor. These efforts will include quantifying the 2-NBDG fluorescence as a function of known concentration injected as well as determining optimal time after injection for data analysis. An accurate and validated algorithm for quantifying 2-NBDG uptake can then be incorporated in Aim 2 to measure metabolic demand, in addition to other biomarkers. Subsequently, we will correlate metabolic demand in tumors with tumor type, receptor status and genomic signatures.

KEY RESEARCH ACCOMPLISHMENTS:

AIM 1
- Demonstrated the potential of using sparse decomposition to analyze HRME images in both preclinical and clinical specimens.
- Determined that radiographic breast density and neoadjuvant chemotherapy affect the optical parameters of benign tissue.
- Surgical margin status is more accurately classified in high density patients and when breast density and neoadjuvant status are known *a priori*.
- Began patient recruitment and imaging with the 2nd generation device and high resolution fluorescence imaging of "hot spots".

AIM 2
- Designed and completed a pilot ex vivo biopsy study which demonstrates the potential of using HRME imaging to diagnose specimens during biopsy procedures.
- Designed and built an integrated probe that combines both the HRME fiber bundle and spectroscopy fibers to acquire spatially co-registrated measurements from all specimen types

AIM 3
- We have demonstrated significant differences in 2-NBDG uptake between tumors exposed to different forms of hypoxia.
- The type of stress experienced by a tumor also affects hemoglobin saturation in the vasculature.

REPORTABLE OUTCOMES:

AIM 1:
1. Torre M. Bydlon, J. Quincy Brown, Stephanie A. Kennedy, Jennifer Gallagher, Marlee Junker, William T. Barry, Joseph Geradts, Lee G. Wilke, Nimmi Ramanujam. "Effects of Radiographic Breast Density on the Optical Properties of Treatment Naive Breast Tissue Margins." ECI – Advances in Optics for Biotechnology, Medicine and Surgery XII. Naples, FL. June 2011.
2. Kennedy, S., et al., *Using wide-field quantitative diffuse reflectance spectroscopy in combination with high-resolution imaging for margin assessment.* Vol. 7890. 2011: SPIE. 78900C.
3. Kennedy, S., et al., *Optical breast cancer margin assessment: an observational study of the effects of tissue heterogeneity on optical contrast.* Breast Cancer Research, 2010. **12**(6): p. R91.
4. Mueller J, Kennedy S, Harmany Z, Mito J, Kim Y, Geradts J, Kortum R, Kirsch D, Willett R, Ramanujam N, Brown JQ, *High resolution vital fluorescence imaging of tumor microanatomy for surgical margin assessment.* Department of Defense Breast Cancer Research Program Era of Hope Meeting, Orlando FL, August 2011.

5. Mueller J, Harmany Z, Mito J, Kennedy S, Kim Y, Geradts J, Kirsch D, Willett R, Ramanujam N, Brown JQ. *Sparse decomposition as a tool for quantitative pathology.* Duke Workshop on

Sensing and Analysis of High-Dimensional Data (SAHD), Duke University, Durham, NC, July 2011.

6. Mueller J, Harmany Z, Mito J, Kennedy S, Kim Y, Geradts J, Kirsch D, Willett R, Ramanujam N, Brown JQ. *High resolution vital fluorescence imaging and analysis of tumor microanatomy for surgical margin assessment*. Advances in Optics for Biotechnology, Medicine, and Surgery XII, Engineering Conferences International, Naples, FL, June 2011.

AIM 2:
1. Leautaud V, Mack V, Wright JN, Lu J, Yu D, Richards-Kortum R: Optical Imaging of Transformed Breast Epithelial Cells and Breast Tumor Microenvironment. In *Biomedical Optics and 3D Imaging Optics and Photonics Congress*. Miami, FL: Optical Society of America; 2010.
2. Ding, H, Lupinacci J, Yang W, Yu D, Richards-Kortum R. High Resolution Optical Microendoscopic Imaging of Breast Cancer. In *Era of Hope-Breast Cancer Research Conference.* Orlando, FL: DOD Defense Health Program; 2011.
3. Leautaud V, Mack V, Wright JN, Lu J, Yu D, Richards-Kortum R: Optical Imaging of Transformed Breast Epithelial Cells and Breast Tumor Microenvironment. In *Era of Hope-Breast Cancer Research Conference.* Orlando, FL: DOD Defense Health Program; 2011.

AIM 3:

1. Rajaram N, Fontanella AN, Frees AE, Millon SR, Hansen K, Jiang TT, Brown JQ, Dewhirst MW, Ramanujam N. "Optical imaging of tumor metabolic response to chronic and cycling hypoxia." Manuscript in preparation.
2. Rajaram N, Frees AE, Jiang TT, Millon SR, Fontanella AN, Dewhirst MW and Ramanujam N. Effect of intermittent hypoxia on vascular oxygenation and tumor glycolytic demand in pre-clinical breast cancer models. Department of Defense Era of Hope Conference, Orlando, FL, Aug 2-5, 2011.
3. Rajaram N, Frees AE, Jiang TT, Millon SR, Fontanella AN, Dewhirst MW and Ramanujam N. Optical molecular imaging of tumor metabolic demand and vascular oxygen saturation: Effect of cycling hypoxia. ECI Advances in Optics for Biotechnology, Medicine and Surgery, Naples, FL, June 5-8, 2011.

CONCLUSIONS:

Aim 1
Preliminary application of sparse decomposition to high resolution images of acriflavine stained tissue shows promise for isolating individual tissue types and ultimately could allow for the automated detection of residual disease of surgical margins. Based on our preliminary analyses, we believe that this image analysis approach is appropriate for HRME detection of residual carcinoma at the surgical margin. In addition we have shown that both radiographic breast density and neoadjuvant status impact the spectroscopic data of the surgical margins and needs to be taken into account when diagnosing surgical margin status. With the implementation of the 49-channel device we will be able to acquire wide-field images of the tumor margins in a shorter amount of time, and be able to do both wide-field imaging and high resolution imaging of suspicious sites which we have implemented in 16 patients. Initial analysis shows potential for using high resolution imaging to further understand the underlying morphology and lead to improved margin assessment.

Aim 2
The *ex vivo* biopsy pilot feasibility study demonstrates that high resolution imaging of acriflavine stained tissue is a potential tool for rapid detection of biopsy positivity in an clinical setting with the goal of aiding in predicting response to therapy. In addition, we have built an integrated probe that will be used in the future to obtain both spectral information and high resolution images. We will characterize and proceed with clinical implementation of this probe in Year 3.

Aim 3
High-resolution imaging of glucose uptake and vascular oxygenation status can provide unprecedented spatial information and help us understand the relationship between both parameters. FDG-PET imaging is currently used in clinics to identify tumor location based on a tumor's avid glucose uptake. However, PET cannot provide information regarding a tumor's likely future course. Our results indicate differences in tumor metabolic response dependent on the type of stress – chronic or cycling hypoxia. Because the type of stress has been linked to long-term tumor behavior, understanding the metabolic response provides us with a vital endpoint that could help predict a tumor's propensity for radio- or chemo-resistance, metastasis or recurrence.

REFERENCES:

1. Farkas, DL, et al. *Preclinical evaluation of nuclear morphometry and tissue topology for breast carcinoma detection and margin assessment*, Breast Cancer Research Treat, 2010.

2. Gareau DS, et al. *Confocal mosaicing microscopy in skin excisions: a demonstration of rapid surgical pathology,* J Microsc, 2009. **233**(1): p.149-59.

3. Gmitro AF, et al. *Computer-aided identification of ovarian cancer in confocal microendoscope images*, JBO, 2008. **13**(2).

4. Muldoon, T.J., et al., *High-resolution imaging in Barrett's esophagus: a novel, low-cost endoscopic microscope,* Gastrointest Endosc, 2008. **68**(4): p. 737-44.

5. Muldoon, T.J., et al., *Subcellular-resolution molecular imaging within living tissue by fiber microendoscop,* Opt Express, 2007. **15**(25): p. 16413-23.

6. Tanbakuchi, A.A., et al., *A clinical confocal microlaparoscope for real-time in vivo optical biopsies,* JBO, 2009. **14**(4): p. 044030.

7. Kirsch, D.G., et al., *A spatially and temporally restricted mouse model of soft tissue sarcoma,* Nat Med, 2007. **13**(8): p. 992-7.

8. Dankort, D., et al., *A new mouse model to explore the initiation, progression, and therapy of BRAFV600E-induced lung tumors,* Genes Dev, 2007. **21**(4): p. 379-84.

9. Gribonval and S. Lesage, *A survey of sparse component analysis for blind source separation: Principles, perspectives, and new challenges*, in 14th European Symposium on Artificial Neural Networks (ESANN) Proceedings, (Bruges, Belgium), pp. 323–330, April 26–28 2006.

10. J.-L. Starck, M. Elad, and D. L. Donoho, *Image decomposition via the combination of sparse representations and a variational approach*, IEEE Transactions on Image Processing, vol. 14, no. 10, pp. 1570–1582, 2005.

11. E. J. Candès and D. L. Donoho, *New tight frames of curvelets and optimal representations of objects with piecewise C^2 singularities*, Communications on Pure and Applied Mathematics, vol. 57, no. 2, pp 219–266, 2004.

12. Conklin, M.W., et al., *Aligned collagen is a prognostic signature for survival in human breast carcinoma*, Am J Pathol, 2011. **178**(3): p. 1221-32.

13. Bydlon, T.M., et al., *Performance metrics of an optical spectral imaging system for intra-operative assessment of breast tumor margins.* Opt. Express, 2010. **18**(8): p. 8058-8076

14. Wilke L.G., et al., *Rapid noninvasive optical imaging of tissue composition in breast tumor margins.* Am J Surg, 2009. **198**(4): p. 566-74.

15. Brown J.Q., et al., *Optical Assesssment of Tumor Resection Margins in the Breast.* Selected Topics in Quantum Electronics, IEEE Journal of, 2010. **16**(3): p. 530-544.

16. Kennedy S., et al., *Optical breast cancer margin assessment: an observational study of the effects of tissue heterogeneity on optical contrast.* Breast Cancer Research, 2010. **12**(6): p. R91.

17. Palmer G.M. and N. Ramanujam, *A Monte Carlo-based inverse model for calculating tissue optical properties. Part I: Theory and validation on synthetic phantoms.* Appl. Opt., 2006. **45**(5): p. 1062-71

18. Palmer G.M., et al., *A Monte Carlo-based inverse model for calculating tissue optical properties. Part II: Application to breast cancer diagnosis.* Appl. Opt., 2006. **45**(5): p. 1072-8.

19. Bender G.M., et al., *A Monte Carlo-based inverse model for calculating tissue optical properties. Part II: Application to breast cancer diagnosis.* Appl. Opt., 2006. **45**(5): p. 1072-8.